17th World Conference on Earthquake Engineering, 17WCEE
Sendai, Japan - September 27th to October 2nd, 2021

The semi-rigid performance of timber connections in Chinese traditional wood-frame structures

Lin Chen(1), Haibei Xiong(2)*, Xiaoming Qing(3), Jie Wang(4)

(1) *Ph. D candidate, Department of Disaster Mitigation for Structures, Tongji University, Shanghai, 200092, China, LinChen_TJ@outlook.com*
(2) ***Corresponding Author,** Professor, Department of Disaster Mitigation for Structures, Tongji University, Shanghai, 200092, China, xionghaibei@tongji.edu.cn*
(3) *Master student, Department of Disaster Mitigation for Structures, Tongji University, Shanghai, 200092, China, xmqin@tongji.edu.cn*
(4) *Master student, Department of Disaster Mitigation for Structures, Tongji University, Shanghai, 200092, China, artemis_pm @163.com*

Abstract

Chinese traditional wood-frame structures have been built for a long history and are still widely constructed in rural areas due to great seismic performance. However, the design method of its lateral resistance system is still not clear. This paper proposed a theoretical model of semi-rigid performance for timber connections in Chinese wood-frame structures. The moment-rotation curve of one common timber connection, namely the mortise and tenon joint, is investigated based on the joint-solution of the geometrical, equilibrium, and physical equations. Furthermore, the influence of the tenon length, tenon height, tenon width, friction coefficient, and joint gap on the moment-rotation curve under direct and inverse force of the mortise and tenon joint has been studied. Results show that the increase of tenon length, tenon width, and friction coefficient can enhance the initial stiffness, yield moment, and ultimate moment of the mortise joint. The tenon height is insensitive to the initial stiffness, while is proportional to the yield moment and ultimate moment. The joint gap has no influence on the initial stiffness, while the rise of the joint gap would weaken the yield moment and ultimate moment. The proposed theoretical moment-rotation has the potential to improve the seismic design of Chinese traditional wood-frame structures.

Keywords: traditional wood frame; timber connections; moment-rotation curve; semi-rigid performance

1. Introduction

Chinese ancient wooden structure is the main structural system of traditional residential buildings for a long history, which is still widely constructed in rural areas. Due to timber being environmental-friendly material, wooden structures have great energy-saving properties and low carbon emission [1,2]. In addition to its excellent seismic performance in previous earthquakes, the Chinese government gives many incentive policies to support the construction of timber structures.

The seismic performance of timber structures mainly benefits from its connection pattern. Timber column and timber beam are connected by the Tenon and mortise joint without mental connectors. Xue [3] et al. discovered the Tenon and mortise joint has great hysteretic behavior by conducting low cyclic loading tests on this joint. Chen [4–6] et al. further validated its semi-rigid performance based on tests of traditional wood frames and proposed a theoretical moment-rotation model. Many other researchers had investigated the mechanical process of the Tenon and mortise joint, and proposed a three-stage model, including elastic stage, yield stage, and plastic stage [7–9]. Besides, Xie [10] et al. investigated the influence of the Tenon shape, and Tenon length on its mechanical performance, and pointed out the bending capacity is sensitive to the Tenon length. However, the theoretical mechanical model based on test results is only applicable to specific materials and sizes. Besides, the high nonlinear characteristics of this joint cannot be accurately reflected by individual tests.

In this paper, the authors propose a theoretical moment-rotation model to predict the semi-rigid performance of the mortise and tenon joint. The deduction of theoretical model is based on the solution of

geometric equation, equilibrium equation, and physical equation, as shown in section 2. To validate the feasibility of the proposed model, a comparison is conducted with experimental data from the literature in section 3. In addition, parameter analysis is also conducted in section 4 to investigate influence factors on mechanical performance of the mortise and tenon joint.

2. Theoretical model

Many experimental studies have shown that the Tenon and mortise joint has great ductility under the lateral force [11]. Thus, both elastic and plastic phases would be studied in the deduction of theoretical model. In each model, three equations, including geometric equation, equilibrium equation, and physical equation are used to solve the moment-rotation curve expression.

Four assumptions are applied to simplify the deduction: (1) Ignoring the deformation of mortise; (2) assuming the Tenon only produces rigid motion; (3) ideal elastic-plastic model is used for the compression in the perpendicular direction of wood; (4) assuming that stress distributed along with the Tenon thickness uniformly.

2.1 Moment-rotation curve under positive force

The size of Tenon and mortise joint is shown in Fig. 1. Assuming that the Tenon rotates around point O under the positive force, the deformation is depicted in Fig. 2.

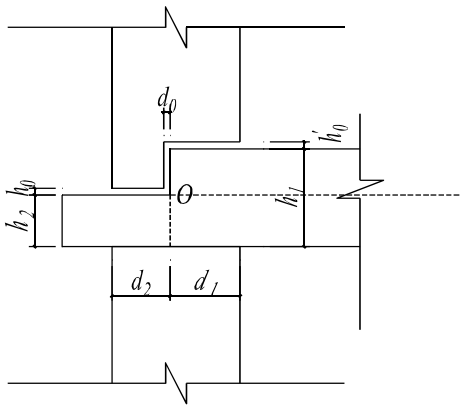

Fig. 1 – The size of Tenon and mortise joint

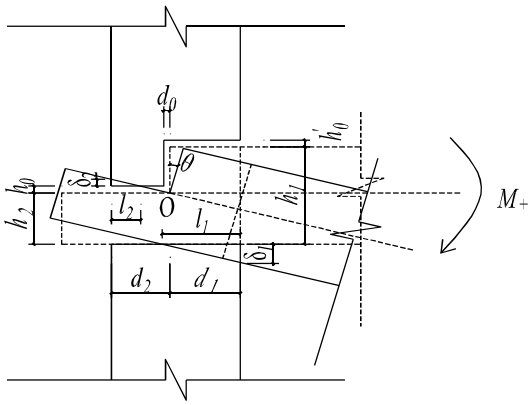

Fig. 2 – Deformation under positive force

According to Fig. 2, geometric equation can be expressed as:

$$l_1 = \frac{\delta_1}{\tan\theta} = d_1 + h_2\left(\frac{1}{\sin\theta} - \frac{1}{\cos\theta}\right) \tag{1}$$

$$l_2 = \frac{\delta_2}{\tan\theta} = d_2 - \frac{h_0}{\tan\theta} \tag{2}$$

Fig. 3 shows the distribution of stress, f_1 and f_2 is sliding friction, assuming μ is the sliding friction coefficient of timber. c_1 and c_2 represent the distance between compression force and point O. The equilibrium equation can be obtained:

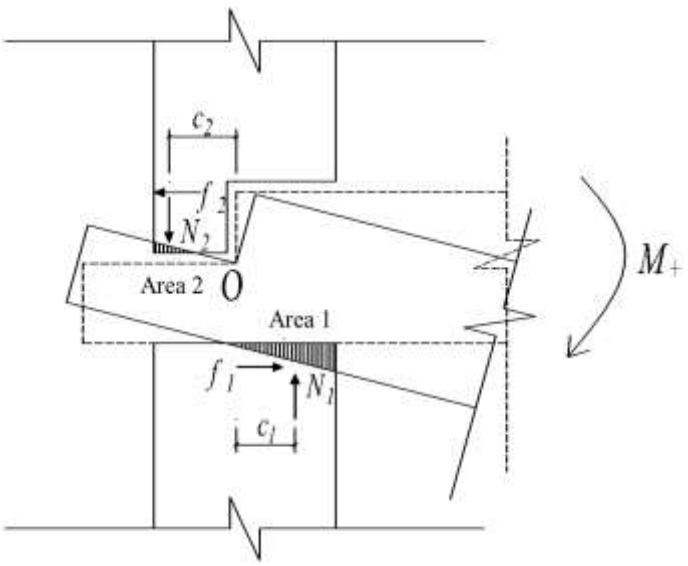

Fig. 3 – Distribution of stress under the positive force.

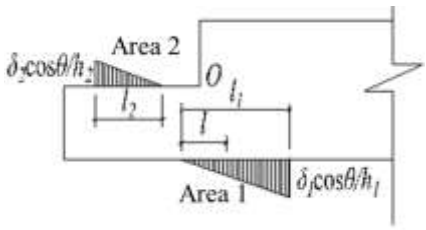

Fig. 4 – Distribution of strain in elastic phase.

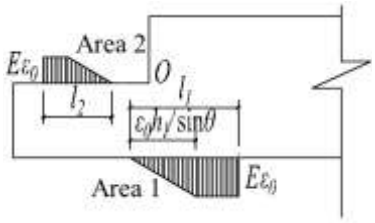

Fig. 5 – Distribution of strain in plastic phase.

$$M_+ = \mu N_1 h_1 + \mu N_2 h_0 + N_1 c_1 + N_2 c_2 \tag{3}$$

In the elastic phase, the distribution of strain of Tenon is shown in Fig. 4. The physical equations can be obtained:

$$N_1 = \int_0^{l_1} \sigma b dl = \int_0^{l_1} E_h \cdot \frac{\delta_1 \cos\theta}{l_1 h_1} l \cdot b dl = \frac{E_h b \delta_1 \cos\theta}{l_1 h_1} \int_0^{l_1} l dl = \frac{E_h b \cos\theta}{2h_1} \delta_1 l_1 \tag{4}$$

$$c_1 = d_1 - \frac{1}{3} l_1 \tag{5}$$

$$N_2 = \frac{E_h b \cos\theta}{2h_2} \delta_2 l_2 \tag{6}$$

$$c_2 = d_2 - \frac{1}{3} l_2 \tag{7}$$

Substitute eq. (4) ~eq. (7) into eq. (3), bending moment of Tenon and mortise joint under positive force in the elastic phase can be expressed as:

$$M_+ = \frac{E_h b}{2h_1}\left[(\mu h_2 + d_1)\delta_1^2 \frac{\cos\theta}{\tan\theta} - \frac{1}{3} \cdot \frac{\cos\theta}{\tan^2\theta}\delta_1^3\right] + \frac{E_h b}{2h_2}\left[(\mu h_0 + d_2)\delta_2^2 \frac{\cos\theta}{\tan\theta} - \frac{1}{3} \cdot \frac{\cos\theta}{\tan^2\theta}\delta_2^3\right] \tag{8}$$

In the plastic phase, the distribution of strain of Tenon is shown in Fig. 5. The physical equations can be obtained:

$$N_1 = E_h \varepsilon_0 b\left(l_1 - \frac{\varepsilon_0 h_1}{\sin\theta}\right) + \int_0^{\frac{\varepsilon_0 h_1}{\sin\theta}} E_h \cdot \frac{l \sin\theta}{h_1} \cdot b dl = E_h b \varepsilon_0 \left(l_1 - \frac{\varepsilon_0 h_1}{2\sin\theta}\right) \tag{9}$$

$$c_1 = d_1 - \frac{l_1^2 + \frac{1}{3} \cdot \frac{\varepsilon_0^2 h_1^2}{\sin^2\theta} - l_1 \cdot \frac{\varepsilon_0 h_1}{\sin\theta}}{2l_1 - \frac{\varepsilon_0 h_1}{\sin\theta}} \tag{10}$$

$$N_2 = E_h b \varepsilon_0 \left(l_2 - \frac{\varepsilon_0 h_2}{2\sin\theta} \right) \tag{11}$$

$$c_2 = d_2 - \frac{l_2^{\,2} + \frac{1}{3} \cdot \frac{\varepsilon_0^{\,2} h_2^{\,2}}{\sin^2\theta} - l_2 \cdot \frac{\varepsilon_0 h_2}{\sin\theta}}{2l_2 - \frac{\varepsilon_0 h_2}{\sin\theta}} \tag{12}$$

Thus, the bending moment of the mortise and tenon joint under positive force in the plastic phase can be expressed as:

$$\begin{aligned} M_+ = {} & f_{c,90} b \left(\mu h_2 + d_1 \right) \left[G(\theta) - \frac{1}{2} H(\theta) \right] - f_{c,90} b \left[\frac{1}{2} G^2(\theta) + \frac{1}{6} H^2(\theta) - \frac{1}{2} G(\theta) H(\theta) \right] \\ & + f_{c,90} b \left(\mu h_0 + d_2 \right) \left[P(\theta) - \frac{1}{2} Q(\theta) \right] - f_{c,90} b \left[\frac{1}{2} P^2(\theta) + \frac{1}{6} Q^2(\theta) - \frac{1}{2} P(\theta) Q(\theta) \right] \end{aligned} \tag{13}$$

Where

$$\begin{cases} G(\theta) = \dfrac{d_1 \sin\theta + h_2 (1 - \cos\theta)}{\sin\theta}, \quad Q(\theta) = \dfrac{f_{c,90} h_2}{E_h \sin\theta} \\ H(\theta) = \dfrac{f_{c,90} h_1}{E_h \sin\theta}, \quad P(\theta) = \dfrac{d_2 \sin\theta - h_0 \cos\theta}{\sin\theta} \end{cases} \tag{13-1}$$

2.2 Moment-rotation curve under reverse force

The deformation of the mortise and tenon joint under reverse force is depicted in Fig. 6. The geometric equation can be expressed as:

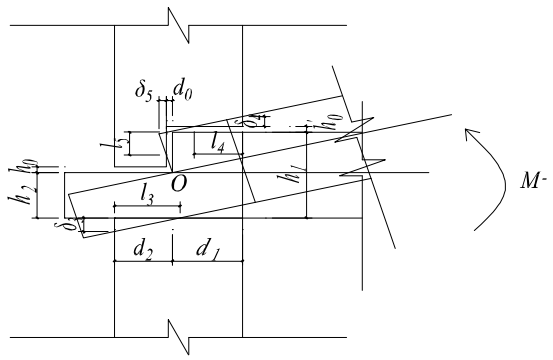

Fig. 6 – Deformation under reverse force

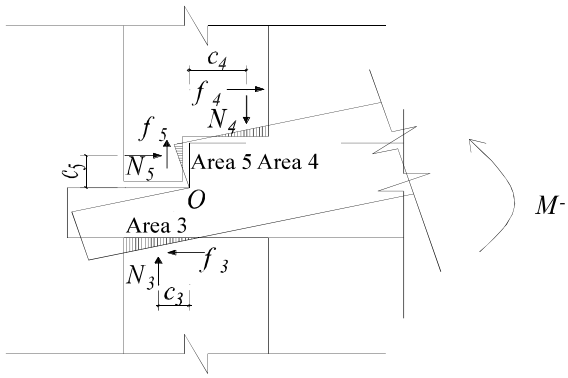

Fig. 7 – Distribution of stress under the reverse force

$$l_3 = \frac{\delta_3}{\tan\theta} = \frac{d_2 \sin\theta + h_2 (1 - \cos\theta)}{\sin\theta} \tag{14}$$

$$l_4 = \frac{\delta_4}{\tan\theta} = \frac{d_1 \sin\theta + (h_1 - h_2)(1 - \cos\theta) - h_0' \cos\theta}{\sin\theta} \tag{15}$$

$$l_5 = \delta_5 \tan\theta + \frac{\delta_5}{\tan\theta} = \frac{(h_1 - h_2)\sin\theta - d_0}{\sin\theta \cos\theta} \tag{16}$$

Under reverse force, three compressional regions exist, and the distribution of stress is shown in Fig. 7. c_3, c_4 and c_5 represents the distance between compression force and point O. The equilibrium equation can be obtained:

$$M_{-} = \mu N_3 h_2 + \mu N_4 \left(h_1 - h_2 + h_0^{'}\right) + \mu N_5 d_0 + N_3 c_3 + N_4 c_4 + N_5 c_5 \tag{17}$$

In the elastic phase, the distribution of strain of Tenon under reverse force is shown in Fig. 8. The physical equations can be obtained:

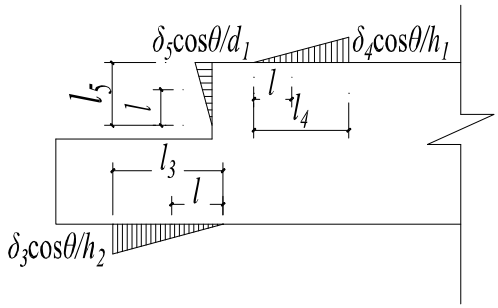

Fig. 8 – Distribution of strain in elastic phase under reverse force.

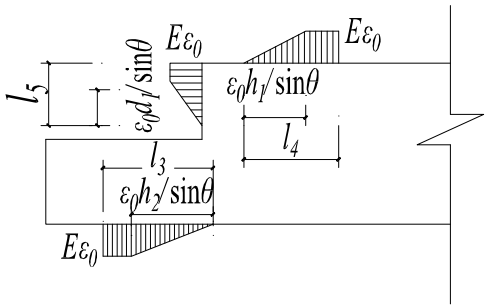

Fig. 9 – Distribution of strain in plastic phase under reverse force.

$$N_3 = \int_0^{l_3} \sigma b dl = \int_0^{l_3} E_h \cdot \frac{\delta_3 \cos\theta}{l_3 h_2} l \cdot b dl = \frac{E_h b \delta_3 \cos\theta}{l_3 h_2} \int_0^{l_3} l dl = \frac{E_h b \cos\theta}{2h_2} \delta_3 l_3 \tag{18}$$

$$c_3 = d_2 - \frac{1}{3} l_3 \tag{19}$$

$$N_4 = \frac{E_h b \cos\theta}{2h_1} \delta_4 l_4 \tag{20}$$

$$c_4 = d_1 - \frac{1}{3} l_4 \tag{21}$$

$$N_5 = \frac{E_h b}{2d_1} \delta_5 l_5 \tag{22}$$

$$c_5 = \left(h_1 - h_2\right)\cos\theta - \frac{1}{3} l_5 \tag{23}$$

Substitute eq. (18) ~eq. (23) into eq. (17), the bending moment of Tenon and mortise joint under reverse force in the elastic phase can be expressed as:

$$\begin{aligned} M_{-} = & \frac{E_h b}{2h_2}\left[\left(\mu h_2 + d_2\right)\alpha(\theta) - \frac{1}{3}\beta(\theta)\right] + \frac{E_h b}{2h_1}\left[\left(\mu\left(h_1 - h_2 + h_0^{'}\right) + d_1\right)\varsigma(\theta) - \frac{1}{3}\xi(\theta)\right] \\ & + \frac{E_h b}{2d_1}\left[\mu d_0 \psi(\theta) + \left(h_1 - h_2\right)\varphi(\theta) - \frac{1}{3}\phi(\theta)\right] \end{aligned} \tag{24}$$

where

$$\begin{cases} \alpha(\theta)=\dfrac{\left[d_2\sin\theta+h_2(1-\cos\theta)\right]^2}{\sin\theta},\beta(\theta)=\dfrac{\left[d_2\sin\theta+h_2(1-\cos\theta)\right]^3}{\sin^2\theta} \\ \varsigma(\theta)=\dfrac{\left[d_1\sin\theta+(h_1-h_2)(1-\cos\theta)-h_0'\cos\theta\right]^2}{\sin\theta},\xi(\theta)=\dfrac{\left[d_1\sin\theta+(h_1-h_2)(1-\cos\theta)-h_0'\cos\theta\right]^3}{\sin^2\theta} \\ \psi(\theta)=\dfrac{\left[(h_1-h_2)\sin\theta-d_0\right]^2}{\sin\theta\cos\theta},\varphi(\theta)=\dfrac{\left[(h_1-h_2)\sin\theta-d_0\right]^2}{\sin\theta},\phi(\theta)=\dfrac{\left[(h_1-h_2)\sin\theta-d_0\right]^3}{\sin^2\theta\cos^2\theta} \end{cases} \tag{25}$$

In the plastic phase, the distribution of strain of Tenon under reverse force is shown in Fig. 9. The physical equations can be obtained:

$$N_3=E_h b\varepsilon_0\left(l_3-\frac{\varepsilon_0 h_2}{2\sin\theta}\right) \tag{26}$$

$$c_3=d_2-\frac{l_3^2+\frac{1}{3}\cdot\frac{\varepsilon_0^2 h_2^2}{\sin^2\theta}-l_3\cdot\frac{\varepsilon_0 h_2}{\sin\theta}}{2l_3-\frac{\varepsilon_0 h_2}{\sin\theta}} \tag{27}$$

$$N_4=E_h b\varepsilon_0\left(l_4-\frac{\varepsilon_0 h_1}{2\sin\theta}\right) \tag{28}$$

$$c_4=d_1-\frac{l_4^2+\frac{1}{3}\cdot\frac{\varepsilon_0^2 h_1^2}{\sin^2\theta}-l_4\cdot\frac{\varepsilon_0 h_1}{\sin\theta}}{2l_4-\frac{\varepsilon_0 h_1}{\sin\theta}} \tag{29}$$

$$N_5=E_h b\varepsilon_0\left(l_5-\frac{\varepsilon_0 d_1}{2\sin\theta\cos\theta}\right) \tag{30}$$

$$c_5=(h_1-h_2)\cos\theta-\frac{l_5^2+\frac{1}{3}\cdot\frac{\varepsilon_0^2 d_1^2}{\sin^2\theta\cos^2\theta}-l_5\cdot\frac{\varepsilon_0 d_1}{\sin\theta\cos\theta}}{2l_5-\frac{\varepsilon_0 d_1}{\sin\theta\cos\theta}} \tag{31}$$

Thus, the bending moment of the mortise and tenon joint under positive force in the plastic phase can be expressed as:

$$\begin{aligned} M_- &= f_{c,90}b(\mu h_2+d_2)\left[E(\theta)-\frac{1}{2}F(\theta)\right]-f_{c,90}b\left[\frac{1}{2}E^2(\theta)+\frac{1}{6}F^2(\theta)-\frac{1}{2}E(\theta)F(\theta)\right] \\ &+f_{c,90}b\left[\mu(h_1-h_2+h_0')+d_1\right]\left[J(\theta)-\frac{1}{2}K(\theta)\right]-f_{c,90}b\left[\frac{1}{2}J^2(\theta)+\frac{1}{6}K^2(\theta)-\frac{1}{2}J(\theta)K(\theta)\right] \\ &+f_{c,90}\mu b d_0\left[M(\theta)-\frac{1}{2}N(\theta)\right]+f_{c,90}b(h_1-h_2)\left[L(\theta)-\frac{1}{2}S(\theta)\right] \\ &-f_{c,90}b\left[\frac{1}{2}M^2(\theta)+\frac{1}{6}N^2(\theta)-\frac{1}{2}M(\theta)N(\theta)\right] \end{aligned} \tag{32}$$

where

$$\begin{cases} E(\theta)=\dfrac{d_2\sin\theta+h_2(1-\cos\theta)}{\sin\theta}, F(\theta)=\dfrac{f_{c,90}h_2}{E_h\sin\theta}, L(\theta)=\dfrac{(h_1-h_2)\sin\theta-d_0}{\sin\theta} \\ J(\theta)=\dfrac{d_1\sin\theta+(h_1-h_2)(1-\cos\theta)-h_0'\cos\theta}{\sin\theta}, K(\theta)=\dfrac{f_{c,90}h_1}{E_h\sin\theta} \\ M(\theta)=\dfrac{(h_1-h_2)\sin\theta-d_0}{\sin\theta\cos\theta}, N(\theta)=\dfrac{f_{c,90}d_1}{E_h\sin\theta\cos\theta}, S(\theta)=\dfrac{f_{c,90}d_1}{E_h\sin\theta} \end{cases} \tag{33}$$

3. Validation with test

To validate the accuracy and rationality of the proposed theoretical model, two sets of test data of literature [12] under positive force and reverse force have been compared with the theoretical M-θ curve. Table 1 lists geometry information and material properties of the test specimen.

Table 1 – Geometry information and material properties of test specimen

h_1 /mm	h_2 /mm	d_1 /mm	d_2 /mm	b /mm	h_0 /mm	h_0' /mm	E_h /MPa	$f_{c,90}$ /MPa	ε_0	μ
180	100	110	100	60	1	1	900	2.9	0.0032	0.4

Fig. 10 and Fig. 11 depict the comparison of theoretical model and test under positive force and reverse force, respectively. It can be observed that the theoretical curve represents the same trend as the test curve. Both of them can be divided into three phases: elastic, stiffness degradation, plastic slip. In the elastic phase, the bending moment is linear with rotation angle. With the increase of bending moment, the Tenon joint enters yield stage, and the stiffness degradation presents obvious nonlinear characteristics. In the plastic slip phase, the bending capacity of the joint is very small, and the increase of rotation angle can hardly raise the bending moment. Furthermore, inflection points are obviously observed in the theoretical curve, while the test curve is relatively smooth. The reason is that a certain Tenon gap is assumed in the theoretical model, and the tenon needs to overcome the gap before it can contact the mortise to produce compressional deformation, which means the compressive region produces deformation in turn. However, in the test, the tenon and mortise are connected before loading because of the self-weight of the beam.

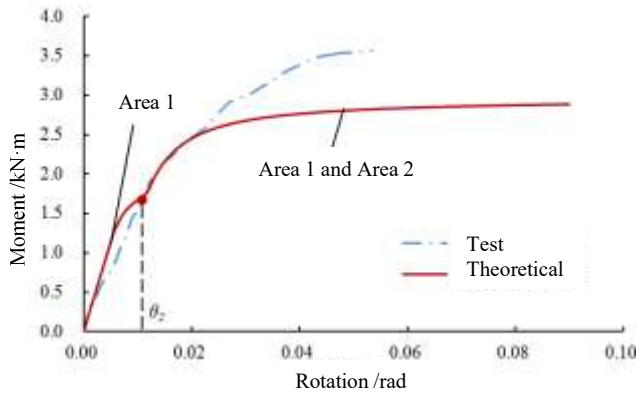

Fig. 10 – Comparison of theoretical model and test under positive force.

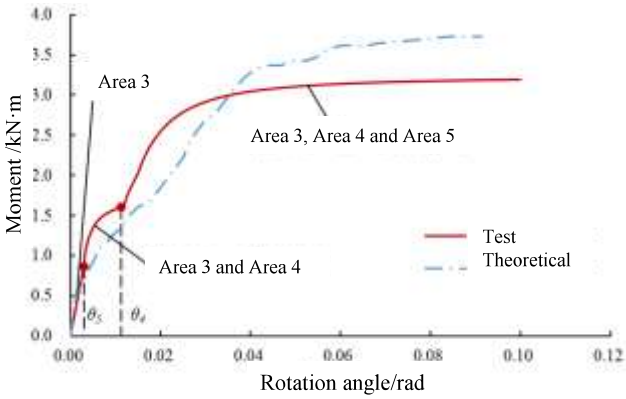

Fig. 11 – Comparison of theoretical model and test under reverse force.

To further investigate the mechanical performance of the theoretical model and test specimen, five factors are defined. Yield moment and yield rotation angle are determined according to the general yield moment method. The ultimate rotation angle and ultimate moment are determined by failure pattern. Under positive force, the failure occurs at the cross section where abrupt variation exists. Under reverse force, the failure occurs at the bottom surface of Tenon. The ductility coefficient is defined as the ratio of ultimate rotation angle and yield rotation angle. Table 2 lists the comparison results. It can be seen that the largest error between the theoretical model and test is less than 30%, representing the theoretical model has a great agreement with tests. The ductility predicted by theoretical model under positive force is larger than that of reverse force, which is consistent with the test results.

Table 2 – Comparison of performance factors between theoretical and experimental values

Factors	Under positive force			Under reverse force		
	theoretical	experimental	error	theoretical	experimental	error
Yield rotation angle /rad	0.018	0.025	28.00%	0.022	0.03	26.67%
Yield moment /kN·m	2.43	2.90	16.21%	2.68	3.21	16.51%
Ultimate rotation angle /rad	0.06	0.06	—	0.08	0.08	—
Ultimate moment /kN·m	2.84	3.38	15.98%	3.17	3.47	8.65%
Ductility coefficient	2.61	2.40	8.75%	2.73	2.67	12.36%

4. Parameter analysis

4.1 Influence of Tenon length

To investigate the influence of Tenon length on the moment-rotation curve, assuming d1 is equal to d2, maintain other factors is the same as table 1, set Tenon length varying from 200 mm to 300 mm. Fig. 12 shows M-θ curve under positive force, and Fig.13 depicts M-θ curve under negative force. With the increase of tenon length, the initial tangent stiffness of M-θ curve gains increase, yield moment, and the ultimate moment also raise gradually. These trends are observed in both positive force and reverse force.

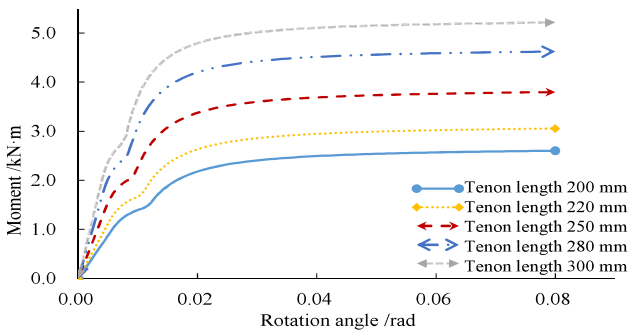

Fig. 12 – Influence of Tenon length on M-θ curve under positive force

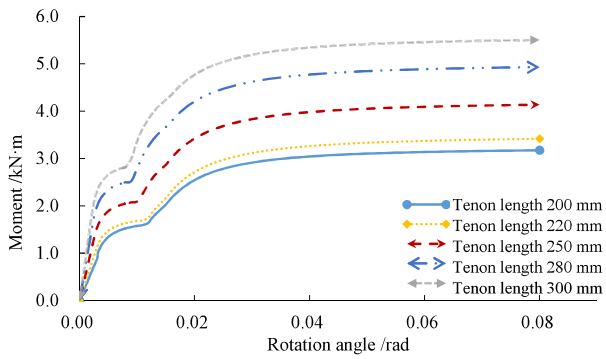

Fig. 13 – Influence of Tenon length on M-θ curve under reverse force

4.2 Influence of Tenon width

To investigate the influence of Tenon width on the moment-rotation curve, maintain other factors is the same as table 1, set Tenon width varying from 60 mm to 100 mm. Fig. 14 shows the influence of Tenon width on M-θ curve under positive force, with the increase of tenon width, initial tangent stiffness of M-θ curve gains short growth, yield moment and ultimate moment increases linearly. These trends are observed in both positive force and reverse force.

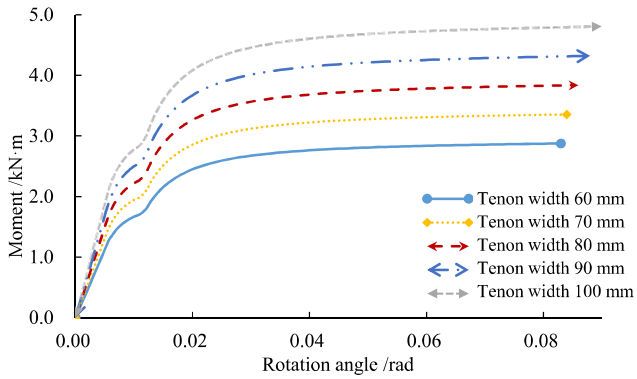

Fig. 14 – Influence of Tenon width on M-θ curve under positive force

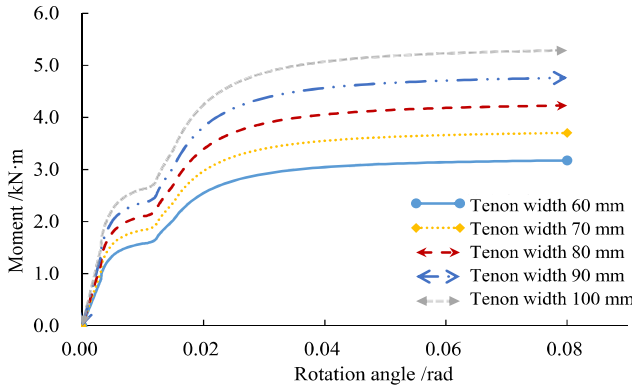

Fig. 15 – Influence of Tenon width on M-θ curve under reverse force

4.3 Influence of Tenon height

To investigate the influence of Tenon height on the moment-rotation curve, assuming h1 is equal to double h2, maintain other factors is the same as table 1, set Tenon height varying from 120 mm to 200 mm. As Fig. 16 shows, with the increase of tenon height, initial tangent stiffness of M-θ curve descends less obviously, yield moment and ultimate moment increases in a small degree. Fig. 17 depicts the same variation pattern under reverse force.

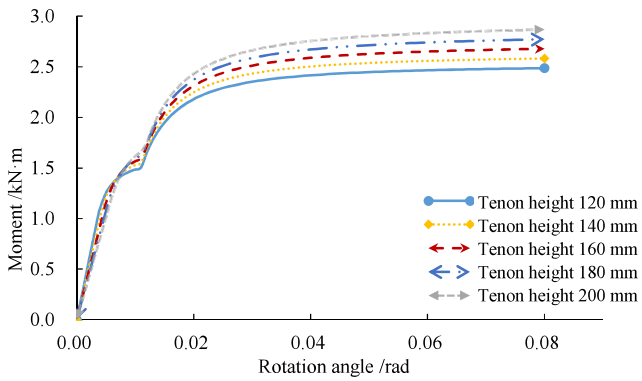

Fig. 16 – Influence of Tenon height on M-θ curve under positive force

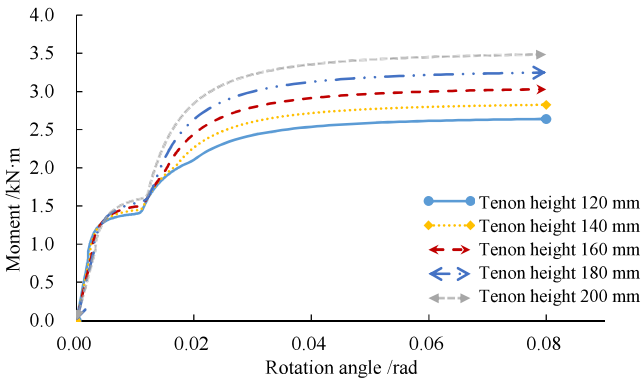

Fig. 17 – Influence of Tenon height on M-θ curve under reverse force

4.4 Influence of friction coefficient

The friction coefficient between timber beam and timber column directly affects interface interaction, causing variation of the seismic performance of timber frame. To investigate the influence of friction coefficient on the moment-rotation curve, maintain other factors is the same as table 1, set friction coefficient varying from 0.1 to 0.6. Fig. 18 shows the influence of friction coefficient on the M-θ curve under positive force. With the increase of friction coefficient, the initial tangent stiffness of M-θ curve gains a certain

growth, yield moment and ultimate moment increases obviously. These trends are observed in the reverse force condition with a small increase amplitude.

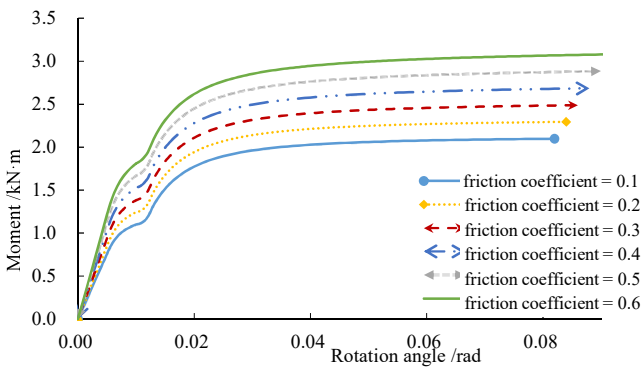

Fig. 18 – Influence of friction coefficient on M-θ curve under positive force

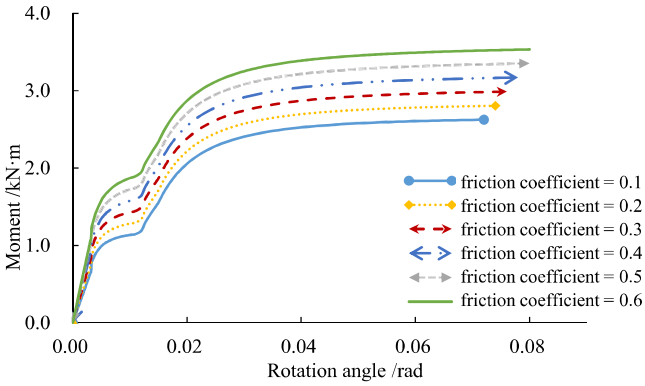

Fig. 19 – Influence of friction coefficient on M-θ curve under reverse force

4.5 Influence of Tenon gap

To investigate the influence of the Tenon gap on the moment-rotation curve, maintain other factors is the same as table 1, set Tenon gap varying from 0 mm to 3 mm. Fig. 20 shows the influence of Tenon gap on M-θ curve under positive force, compared with Tenon gap at 0 mm, the existence of Tenon gap would cause a decrease of the initial tangent stiffness. However, when the Tenon gap exists, with the increase of it, the initial tangent stiffness shows no variations, yield moment and ultimate moment decreases, and the reduction range of yield moment exceeds that of the ultimate moment. These trends are observed in the reverse force condition.

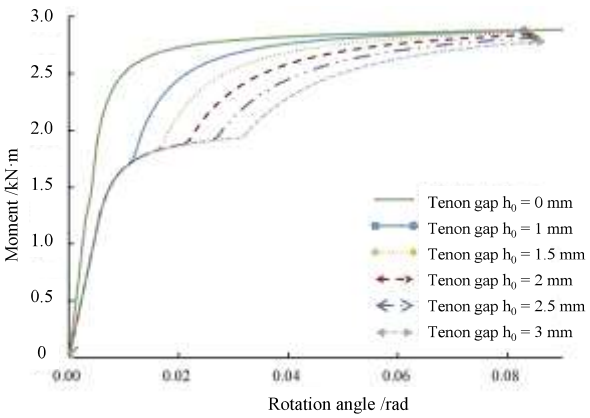

Fig. 20 – Influence of Tenon gap on M-θ curve under positive force

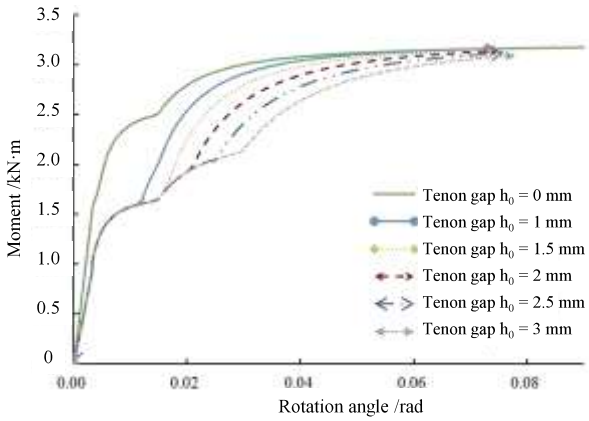

Fig. 21 – Influence of Tenon gap on M-θ curve under reverse force

5. Conclusion

The authors propose a theoretical moment-rotation model of the Tenon and mortise joint for traditional wood frame structures based on the solution of the geometric equation, equilibrium equation, and physical equation. Experimental data from literatures validates the feasibility of the proposed model to predict bending capacity under both positive force and reverse force with relatively high accuracy. Parameter analysis shows that the increase of tenon length, tenon width, and friction coefficient can raise initial stiffness, yield moment, and ultimate moment. The tenon gap has no obvious influence on the initial stiffness. With the increase of the tenon gap, yield moment and ultimate moment would decrease.

6. Acknowledgements

The authors greatly appreciate the funding support from the Fundamental Research Funds for the Central Universities (Grant number 22120190229).

7. References

[1] Xiong HB, Zhang C, Yao JT, Zhao Y (2011): Environmental Impact Comparison of Different Structure Systems Based on Life Cycle Assessment Methodology. *Advanced Materials Research*, **374–377**, 405–411.

[2] O'CONNOR J, DANGERFIELD J (2004): The Environmental Benefits of Wood Construction. In: *8th World Conference on Timber Engineering(WCTE 2004) vol.1: Presentations held on Monday*.

[3] Xue J, Xu D, Xia H (2018): Experimental Study on Seismic Performance of Through-Tenon Joints with Looseness in Ancient Timber Structures. *International Journal of Architectural Heritage*, **14**(4), 1–13.

[4] Chen CC, Qiu HX, Xu MG (2014): Experimental Study on Flexural Behavior of Typical Mortise-Tenon Joints. *Applied Mechanics and Materials*, **578–579**, 160–163.

[5] Chen C, Qiu H, Lu Y (2016): Flexural behaviour of timber dovetail mortise–tenon joints. *Construction and Building Materials*, **112**, 366–377.

[6] Chen LK, Li SC, Wang YT, *et al.* (2017): Experimental Study on the Seismic Behaviour of Mortise–Tenon Joints of the Ancient Timbers. *Structural Engineering International*, **27**(4), 512–519.

[7] Huang H, Wu Y, Li Z, Sun Z, Chen Z (2018): Seismic behavior of Chuan-Dou type timber frames. *Engineering Structures*, **167**, 725–739.

[8] Qing C, Zhi Y, Jianwu P (2011): Experimental study on seismic characteristics of typical mortise-tenon joints of Chinese southern traditional timber frame buildings. *ence China Technological ences*, (09), 2404–2411.

[9] Huang H, Sun Z, Guo T, Li P (2017): Experimental Study on the Seismic Performance of Traditional Chuan-Dou Style Wood Frames in Southern China. *Structural Engineering International*, **27**(2), 246–254.

[10] Qifang X, Peijun Z, Wei X, Yazhen C, Fengliang Z (2014): Experimental study on seismic behavior of damaged straight mortise-tenon joints of ancient timber buildings. *Journal of Building Structures*, **35**(11), 143–150.

[11] Xiaowei, Li, Junhai, *et al.* (2015): Experimental Study on the Traditional Timber Mortise-Tenon Joints. *Advances in Structural Engineering*, **18**(12), 2089–2102.

[12] Zhao H, Dong C, Xue J The experimental study on the characteristics of mortise-tenon joint historic timber buildings. *Journal of Xi'an University of architecture and technology (Natural Science Edition)*, **42**(3), 315–318.

